

Spatially Resolved Measurements in a Stagnation-Flow Reactor: Kinetics of Catalytic NH₃ Decomposition

Sadaf Davari, Camilo Cárdenas, Matthias Hettel, Patrick Lott, Steffen Tischer, Sofia Angeli and Olaf Deutschmann*

DOI: 10.1002/cite.202400100

 This is an open access article under the terms of the [Creative Commons Attribution](#) License, which permits use, distribution and reproduction in any medium, provided the original work is properly cited.

Dedicated to Prof. Dr.-Ing. Andreas Seidel-Morgenstern on the occasion of his retirement

A stagnation-flow reactor was employed to investigate the decomposition of ammonia over a Ni/Al₂O₃ catalyst across a range of system pressures and ammonia mole fractions. The results indicate that the system pressure has a negligible impact on the light-off behavior and the concentration profiles of NH₃. A comparison of 1D modelling with 3D computational fluid dynamics (CFD) computations justifies the use of the simpler flow model. Good agreement between experiments and the 1D simulation is achieved for two different kinetic models from literature in the mainly diffusion-controlled regime. For lower temperatures, at which the process is kinetically controlled, the two mechanisms exhibit significant differences. The stagnation-flow reactor concept is shown to be a promising tool for understanding, developing, and validating the reaction kinetics of heterogeneous catalytic processes.

Keywords: Ammonia decomposition, Heterogeneous kinetics, Nickel catalyst, Stagnation-flow reactor

Received: July 26, 2024; *revised:* October 24, 2024; *accepted:* October 25, 2024

1 Introduction


The development and validation of detailed surface reaction mechanisms typically requires a comparison of experimental data with numerical simulations for different reactor configurations. One of the main difficulties in determining reaction kinetic parameters is the superimposed influence of mass and heat transport. Often simplifications are assumed to minimize computational obstacles. In this regard, reducing the dimensionality of a physical system is a possibility to diminish the effort for both experimental investigation and numerical modeling. On the one hand, the usage of a system, where data have to be sampled along a single coordinate only is preferable because the collection is faster. On the other hand, the modeling is easier and the computational time is reduced, which is of particular importance for reactive systems in which a large number of species are involved.


A stagnation-flow reactor (SFR) is a useful tool for kinetic measurements because it exhibits a well-defined flow field that enables the investigation of heterogeneous chemistry on catalyst surfaces. For modeling, the Navier-Stokes equations, together with thermal energy and species continuity equations, can be transformed into a 1D boundary-layer problem [1–3]. This enables a fast numerical calculation.


The main characteristics of a stagnation flow field is illustrated in Fig. 1. A stagnation plate is positioned per-

pendicular inside a homogeneous laminar parallel flow. The resulting flow field near the plate is axisymmetric and depends only on the two coordinates z (axial distance from the surface) and r (radial coordinate). The path line of the flow on the symmetry axis ends at the stagnation point on the plate. There, the axial velocity u_z is zero. The boundary layer thickness δ with respect to the axial component of the flow u_z is defined as the distance to the surface where the velocity has dropped by more than 1 % from the respective values in the far field [4]. A unique characteristic of such a flow field is that the boundary layer thickness of axial

¹Sadaf Davari, ¹Dr. Camilo Cárdenas

 <https://orcid.org/0009-0008-3261-9947>, ¹Dr. Matthias Hettel

 <https://orcid.org/0000-0001-7869-1989>, ¹Dr. Patrick Lott

 <https://orcid.org/0000-0001-8683-2155>, ²Dr. Steffen Tischer

 <https://orcid.org/0000-0002-9272-5556>, ²Dr. Sofia Angeli

 <https://orcid.org/0000-0001-8623-047X>,

^{1,2}Prof. Dr. Olaf Deutschmann

 <https://orcid.org/0000-0001-9211-7529> (deutschmann@kit.edu)

¹Institute for Chemical Technology and Polymer Chemistry (ITCP), Karlsruhe Institute of Technology (KIT), Engesserstr. 20, 76131, Karlsruhe, Germany.

²Institute of Catalysis Research and Technology (IKFT), Karlsruhe Institute of Technology, Hermann-von-Helmholtz-Platz 1, 76344, Eggenstein-Leopoldshafen, Germany.

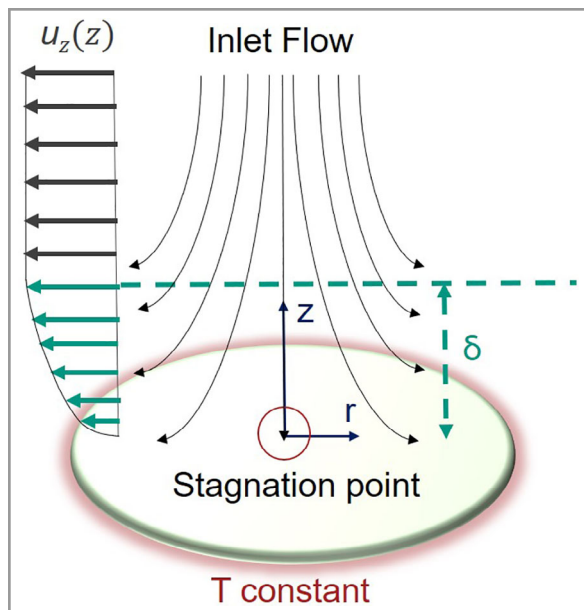


Figure 1. Characteristics of the flow field in a stagnation flow reactor over a flat plate, which is coated with a catalyst in the present study.

velocity, temperature, and concentrations in the axial direction z are independent from the radial coordinate r . Hence, a measurement of profiles along a line in axial direction can in principle be conducted at any radial position r .

In the 1980s, Kee et al. described in detail the 1D model for a stagnation flow based on the simplifications of the Navier-Stokes equations. Their pioneering work laid the foundation for using SFRs to study flame structures and combustion chemistry [3, 5]. Subsequently, a variety of studies have explored mathematical modeling [6], fluid flow effects [7, 8], transport phenomena [9], fluid dynamics [10], dynamic optimization [11], and the thermophysical properties [12] of this type of reactors from a numerical perspective. Furthermore, Lam et al. [13] investigated the physical concerns, model equations, and algorithms associated with SFRs. Later, Li et al. examined the physics and chemistry outcomes of it [14]. In 2008 [15] and 2014 [16], comparative studies analyzed the differences between 1D SFRs and 2D systems such as packed-bed reactors, further advancing the understanding and application of these models. Moreover, numerous simulations have been conducted to investigate chemical vapor deposition (CVD) processes [17], combustion reactions involving volatile organic compounds (VOCs) [18], hydrogen [19], carbon monoxide [20], silicon [21], methane [22], and propane, and reforming of the latter [23]. Wehinger [24] performed a 3D computational fluid dynamic (CFD) modeling of an SFR for dry reforming of methane. The calculation results fitted very well with experimental data as well as with 1D calculations by McGuire et al. [25].

Experiments have made an important advancement to the knowledge and use of SFRs along with modeling studies. By

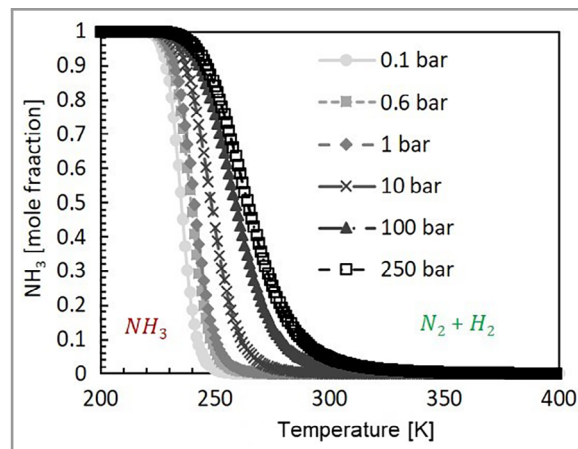


Figure 2. Equilibrium composition as function of temperature and pressure for ammonia and hydrogen/nitrogen.

implementing the ideas developed by Kee et al. [3] to perform tests in a scalable SFR, Hahn et al. confirmed them in 1996 [26]. Two years later, Kim et al. reported experimental data obtained in a vertical SFR for the first time [27]. According to experiments by Chae et al. “The SFR design supplies not only well-behaved, uniform flow, leading to uniform growth rates across the substrate, but also an inherently simple reactor geometry that can be simulated using one-dimensional reacting flow models” [28]. Rice et al. [29] studied methane oxidation in 2007 using the SFR’s down-flow orientation. McGuire et al. (2009) [30] and Karakaya et al. (2013, 2016) [1, 31] investigated methane reforming over a rhodium catalyst in the SFR.

We have a long history of studies in stagnation flow (SFR), with substantial experience gained over the years using the simplified 1D stagnation flow field model to describe the oxidation behavior of CH_4 , CO , and H_2 , as well as CH_4/H_2 mixtures [1, 20, 32–35]. In the present work, the SFR was used to investigate catalytic decomposition of ammonia.

Ammonia (NH_3) decomposition, Eq. (1), has recently gained increasing interest in relation to storage of green hydrogen. Ammonia is composed of 17.73 wt % hydrogen, it can be liquified at relatively moderate conditions ($-33\text{ }^\circ\text{C}$ at atmospheric pressure or at 8 bar at room temperature [36]), making it easier to store and transport compared to pure hydrogen. Upon reaching its destination, ammonia can be decomposed to release hydrogen, offering a flexible and efficient supply chain.

The industrial decomposition of ammonia into nitrogen and hydrogen is an endothermic process, typically requiring high temperatures (between $800\text{ }^\circ\text{C}$ and $950\text{ }^\circ\text{C}$ using a nickel-based catalyst) [37, 38]. Fig. 2 shows the thermodynamic equilibrium for ammonia decomposition computed by the DETCHEM^{EQUIL} [39] software. The endothermic decomposition reaction is known to be favored at low temperature and low pressure [40]. From a kinetic perspective, higher temperatures are necessary for practical applications,

as the decomposition is typically required to be fast [38].



Catalysts play a crucial role in accelerating the ammonia decomposition process. Since 1904, various catalysts along with different techniques have been explored for ammonia decomposition [37]. In the literature, the decomposition capacity of various metals has been explored, among which iron (Fe), ruthenium (Ru), and nickel (Ni) have comparably low activation energies [38], with Ru being on the top of the volcano curve [41]. Nevertheless, due to the high price of ruthenium – a noble metal that is limited in nature – low-cost catalytic compositions with similar activity to that of ruthenium have been strongly requested. In the context of environmental sustainability, it is advised to consider the environmental impact of the material used, such as its global warming potential or the energy required for its extraction and refining, in addition to the price of the metal on which the catalyst is based.

In their review paper on ammonia decomposition, Lucentini et al. [37] explore the connection between the cost of the various elements and their potential impact on global warming over a century. Given all aspects, nickel is a highly attractive alternative to ruthenium. Muroyama et al. [42] prepared a variety of nickel catalysts supported on metal oxides in 2012 and studied their catalytic activity for ammonia decomposition; because of the high surface area of the alumina (Al_2O_3) support, the Ni/ Al_2O_3 catalyst achieved the highest ammonia conversion among the catalysts examined. In 2021, Andache et al. [43] described how nickel interacts with alumina depending on the nickel loading (5–15 %) and found that a higher nickel loading could potentially result in more active sites on the surface due to the presence of agglomerated NiO particles.

In this work, we use a 20 wt % Ni/ Al_2O_3 catalyst to investigate the catalytic decomposition of ammonia in an SFR at different conditions. Numerical simulations employing detailed microkinetic models reveal the potential of the SFR in the investigation of catalytic reactions. Spatially resolved concentration profiles perpendicular to the catalytic surface are obtained by a capillary technique and discussed in comparison with modeling data, highlighting the unique ability of the

SFR to allow profile measurements within the boundary layer.

2 Stagnation-Flow Reactor

2.1 Laboratory-Scale Experimental Setup

The catalytic activity measurements were carried out in a stagnation-flow reactor, which was also used in previous studies [1, 31, 44]. Fig. 3 presents a schematic illustration of the SFR reactor. The incoming flow is homogenized with a three-layer arrangement. The stagnation surface is given by a solid ceramic disk of 56 mm in diameter and 6 mm thickness, which is produced by using a high-temperature castable ceramic resin and hardener (COT Rescor 780, Cotronics Corp.). The resulting structure consists of 99 wt % Al_2O_3 . An R-type thermocouple (rhodium-platinum) with 0.2 mm thickness (TC direct) crosses from backwards to a position near the surface of the disk to monitor and control its temperature. The disk is heated using a resistive heater, which is placed on the back of the disk and which is made out of Kanthal A1, a ferritic iron-chromium-aluminum

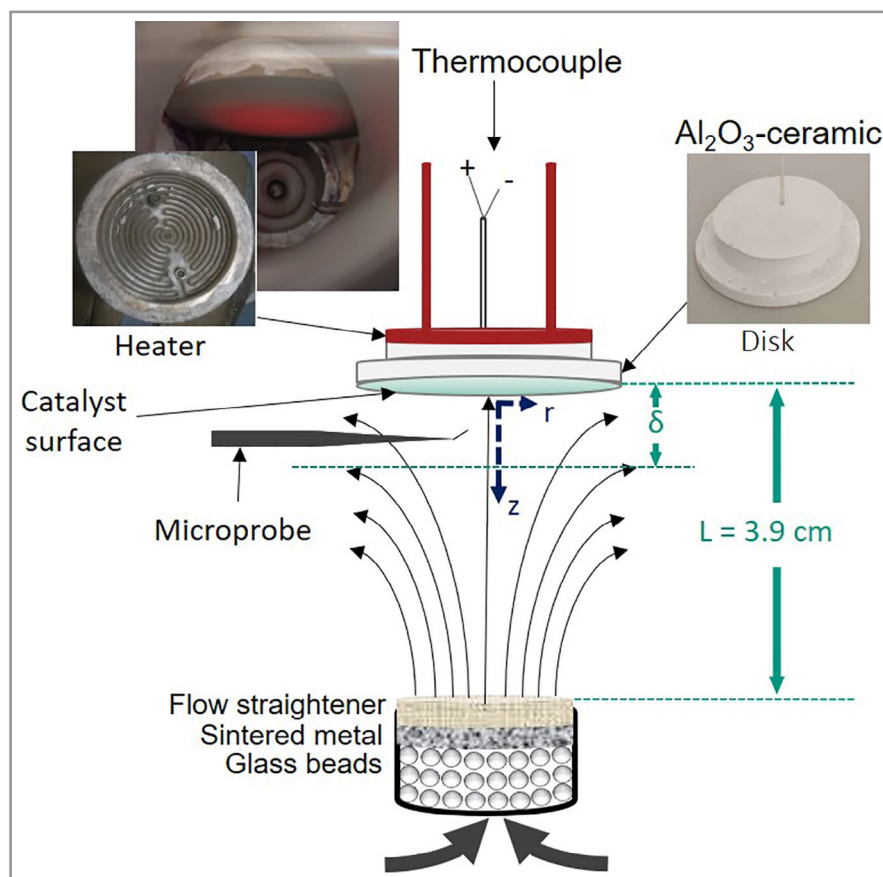


Figure 3. Sketch of the experimental setup of the stagnation-flow reactor with catalytic surface (light green).

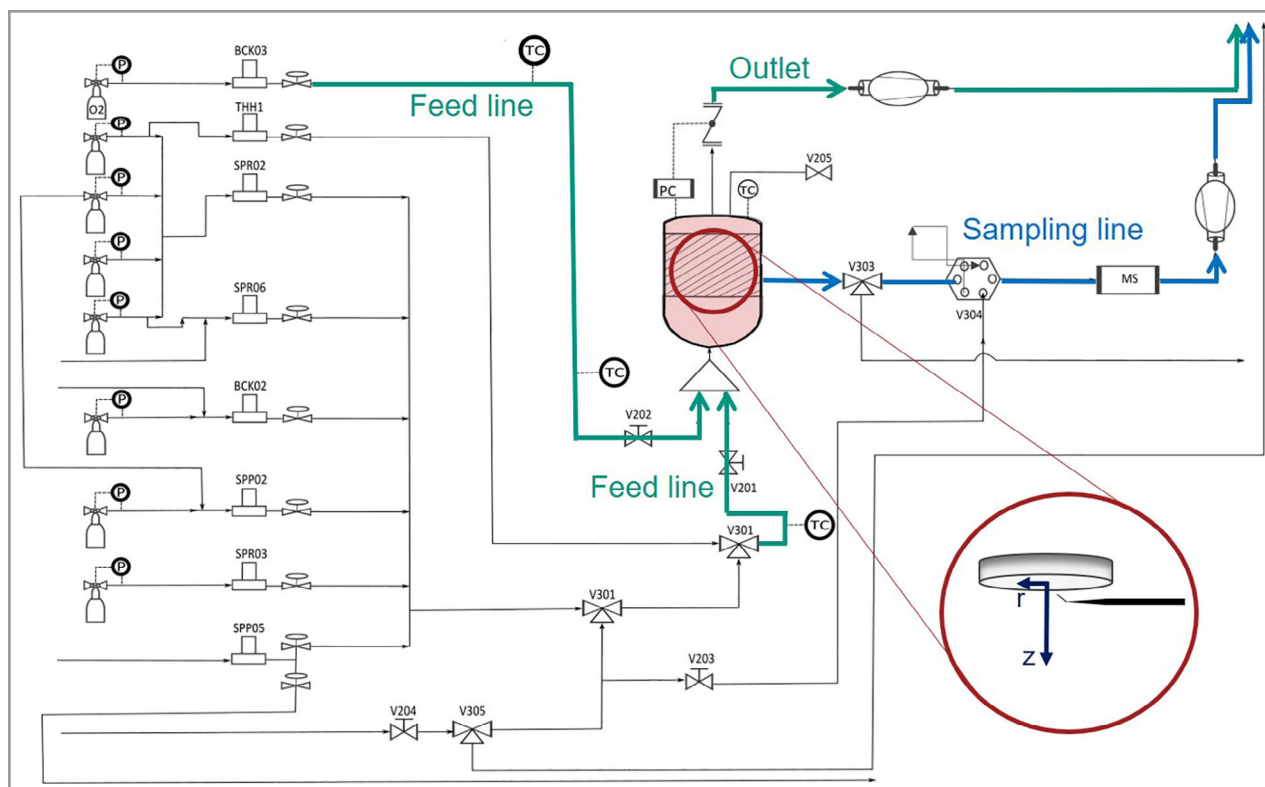


Figure 4. Process flow diagram of the experimental setup.

alloy (Sandvik Materials Technology) cut to a specific shape that ensures a homogeneous heat distribution on the disk. The power applied to the heater is controlled by a PID unit (Eurotherm 818). The other side of the disk, the one oriented to the flow, represents the catalytic surface.

Using a capillary sampling technique, probes of the gas phase were sampled in order to determine the concentration profiles within the boundary layer. The microprobe capillary (Hilgenberg GmbH with 50 μm opening and 15° bend angle) can be positioned very close to the catalytic surface and moved perpendicular to the surface of the plate into the axial direction of the flow. The radial distance from the stagnation point is fixed at 8 mm from the center of the catalytic surface. The position of the microprobe in the boundary layer is controlled by a step motor (MDrive23, Schneider Electronic SE). The gas composition for every axial position is analyzed by a mass spectrometer, MS (HPR20, Hiden Analytical). The MS signal was monitored using the MASsoft 10.0 software (Hiden Analytical) and the obtained data were processed using an in-house code written in Matlab. Compared to the temperature signal, it is notable that the data recorded by the MS is subject to a delay of 300 s. The origin of the coordinate system is allocated in the center of the disk in its coated surface (Fig. 3).

Fig. 4 displays the process flow diagram of the SFR setup. The reaction gas feeding system consists of seven mass flow

controllers that allow to feed various gases into the reactor. Note, that argon was used as inert carrier gas throughout the ammonia decomposition experiments presented in this study. The pressure-sealed containment includes a unique-design mixing chamber and the stagnation flow device. The diameter of the flow inlet is 3.75 cm, and it is positioned 3.9 cm apart from the ceramic disk. Throughout the containments presented herein, the pressure inside the reactor is maintained by a vacuum pump (Edwards xdi10) and a butterfly valve (MKS T3BIA).

2.2 Modeling and Simulation

2.2.1 3D Modeling

For 3D modeling, the CFD code FLUENT was used [45]. The program solves the Navier-Stokes equations together with transport equations for energy and species. Kinetic theory was applied for the calculation of fluid properties. The SIMPLE (Semi Implicit Pressure Linked Equations) algorithm together with second-order discretization schemes were applied for the solution process.

The calculation comprised one quarter of the SFR (Fig. 5). The inlet flow region is marked in red and the annular gap for outflow in blue. On both regions some velocity vectors are added. The catalytic plate is colored in turquoise. The top boundary around the inlet and the circumferential

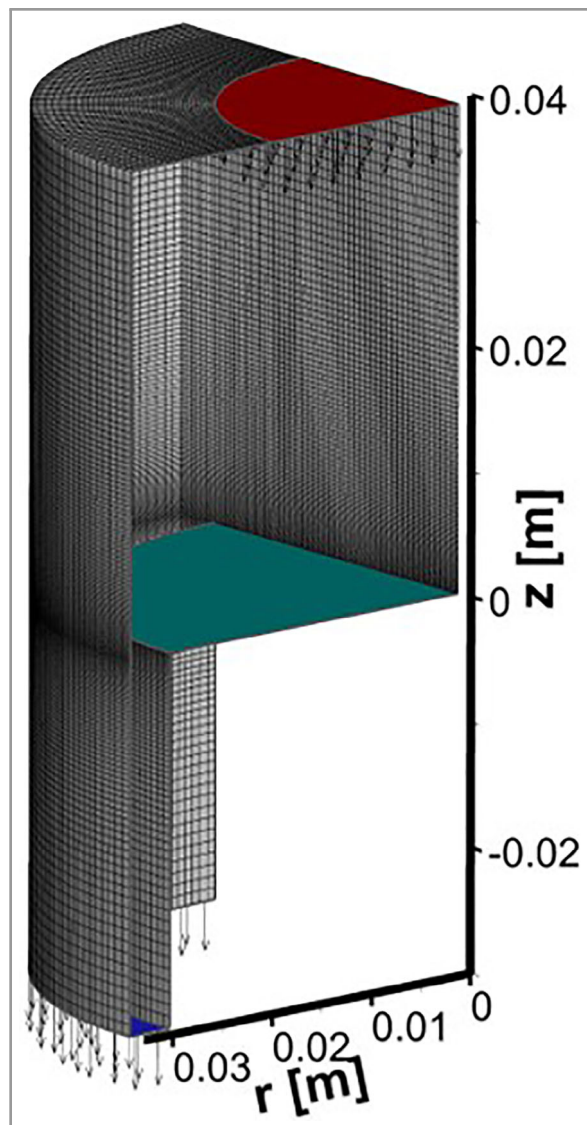


Figure 5. Computational domain for 3D calculation.

boundary were defined as adiabatic walls. The two inter-section areas in circumferential direction were defined as symmetry planes. The boundary conditions for inlet and outlet are given in Tab. 1.

Table 1. Inlet/outlet boundary conditions.

Quantity	Inlet	Outlet
Ar [vol.-%]	99.9	zero grad.
NH ₃ [vol.-%]	0.1	zero grad.
T [°C]	40	zero grad.
<i>u_z</i> [m s ⁻¹]	-0.176	zero grad.
<i>p</i> [mbar]	zero grad.	900

2.2.2 1D Modeling

In general, a 1D model is sufficient for the numerical simulation of the stagnation flow reactor if all design parameters are carefully taken into account. Therefore, later, in Sect. 4.3 the experimental data will be compared with numerical results from the code DETCHEM^{STAG}, which solves the 1D equations of the stagnation flow system [39].

Eqs. (2), (3), and (4) correspond to the species mass fractions, continuity equation, and momentum in the gas phase, respectively. Eq. (5) is the condition for the eigenvalue of the momentum, and the equation of state for ideal gas is used (Eq. (6)).

$$\frac{\partial Y_i}{\partial t} = -\frac{\rho v_x}{\rho} \frac{\partial Y_i}{\partial x} + \frac{1}{\rho} \dot{\omega}_i M_i - \frac{1}{\rho} \frac{\partial j_i}{\partial x} \quad (2)$$

$$0 = \frac{p}{R} \frac{\bar{M}^2}{T^2} \left(T \sum_{i=1}^{N_g} \frac{\partial_t Y_i}{M_i} + \frac{\partial_t T}{\bar{M}} \right) - 2\rho V - \frac{\partial(\rho v_x)}{\partial x} \quad (3)$$

$$\frac{\partial V}{\partial t} = -\frac{\rho v_x}{\rho} \frac{\partial V}{\partial x} - V^2 - \frac{\Lambda}{\rho} + \frac{1}{\rho} \frac{\partial}{\partial x} \left(\mu \frac{\partial V}{\partial x} \right) \quad (4)$$

$$0 = \frac{\partial \Lambda}{\partial x} \quad (5)$$

$$\rho = \frac{p \bar{M}}{RT} \quad (6)$$

Here, mass fractions are represented by Y_i , the molar mass by M_i , the density by ρ , the axial velocity by v_x , the pressure by p , the temperature by T , the mixture viscosity by μ , and the gas phase reaction rate by $\dot{\omega}_i$. V stands for a scaled radial velocity and Λ is an eigenvalue of the radial momentum equation. The temperature and species equations also include the diffusion velocity of each species. A mixture-averaged diffusion equation is employed to calculate diffusive fluxes, consisting of Fick's diffusion and thermal diffusion (Eq. (7)). However, these terms need correction to guarantee the zero-net flow (Eq. (8)). Here, N_g stands for the gas-phase species in the equations, $D_{i,M}$ is the averaged diffusion, and D_i^T is the thermal diffusion coefficient of each species.

$$\hat{j}_i = - \left(\rho D_{i,M} \frac{Y_i}{X_i} \frac{\partial X_i}{\partial x} + \frac{D_i^T}{T} \frac{\partial T}{\partial x} \right) \quad (7)$$

$$j_i = \hat{j}_i - Y_i \sum_{k=1}^{N_g} \hat{j}_k \quad (8)$$

Surface reaction and diffusion in washcoats is accounted for by an additional source term in the boundary cell (with width Δx^+).

$$\rho \frac{\partial Y_i}{\partial t} \Delta x^+ = -j_i + \rho u Y_i + \eta F_{\text{cat/geo}} s_i M_i \quad (9)$$

where η is the effective factor of the mixed (molecular and Knudsen) washcoat diffusion for ammonia as rate-limiting

species (based on the Thiele modulus [19]), $F_{\text{cat/geo}}$ is the surface enlargement factor (ratio of catalytically active surface area to the geometric surface area), and \dot{s}_i are the surface reaction rates. Surface adsorption and desorption processes can result in a Stefan velocity, in particular during transients

$$u_{\text{surf}} = \frac{1}{\rho} \sum_{i=1}^{N_g} \dot{s}_i M_i \quad (10)$$

which serves as a boundary condition for the axial velocity at the gas-surface interface.

The presumption of the derivation of the 1D equations above was that the flow is nearly inviscid over most of the domain, whereas viscous and diffusive transport effects become important in a thin region near the surface where a boundary layer is formed. For isothermal flow without reaction there is only a velocity boundary layer. When considering reactions, there are also boundary layers for temperature and species concentration. The thickness of the fluid boundary layer can be described by Eq. (11).

$$\delta_f = \frac{z}{Re^{0.5}} \cdot \left[\frac{0.2365}{Re^{0.5}} + \left(1.892 + \frac{0.0559}{Re} \right)^{0.5} \right] \quad (11)$$

$$Re = \frac{L \cdot u_z}{\nu} \quad (12)$$

with L as the gap height [47], u_z as the axial velocity at the inlet, and ν as the kinematic viscosity of the fluid. Even though Eqs. (2), (4), and (9) are written in transient formulation for numerical stability, only the steady-state solution is evaluated.

2.3 Catalyst Synthesis and Characterization

2.3.1 Catalyst Preparation

The incipient wetness impregnation method was applied to prepare the catalyst. $\text{Ni}(\text{NO}_3)_2 \cdot 6(\text{H}_2\text{O})$ was dissolved in deionized water and the resulting solution was used to impregnate Ni onto the $\gamma\text{-Al}_2\text{O}_3$ support material that exhibits a pore volume of 0.95 mL g^{-1} . Four impregnation steps were necessary and the powder was dried for 6 h at $75 \text{ }^\circ\text{C}$ between each step. Once the target loading of 20 wt % Ni was achieved, the obtained catalyst powder was calcined for 5 h at $500 \text{ }^\circ\text{C}$.

Subsequently, a slurry was prepared by mixing 1.8 g of the catalyst powder and 0.2 g of Disperal P2 (Sasol) with approx. 12 mL of water. After milling of this mixture for 5 min at 500 rpm in two sets, with 15 min of rest in between, a spin spray technique was employed to apply the slurry onto a solid reactor plate in the form of a stagnation disk; finally, the washcoated disk was calcined for 5 h at $550 \text{ }^\circ\text{C}$. Here-with, a smooth washcoat layer with a thickness of $100 \text{ }\mu\text{m}$ (cf. Sect. 4.2) and a porosity of 0.52 was obtained.

2.3.2 Catalyst Characterization

In this study, several characterization techniques were employed to analyze the properties of the catalyst. Ex-situ X-ray diffraction (XRD) was applied to determine the crystalline structure and phase composition of the mentioned catalyst. The XRD pattern is recorded with a D8 Advance diffractometer (Bruker) using Cu K- α radiation (Cu K- $\alpha 1 = 1.5406 \text{ \AA}$; Cu K- $\alpha 2 = 1.5666 \text{ \AA}$) over the 2θ range of 10° to 120° , with a step size of 0.017° . The instrument was operated at 40 mA and 40 kV. Data analysis and background subtraction were performed using the Diffrac.EVA software.

The specific surface area of the support and the catalyst was obtained by means of N_2 -physisorption measurements that were evaluated according to the Brunauer-Emmett-Teller (BET) method. For this, nitrogen adsorption-desorption isotherms were obtained at 77 K using a BELSORP Mini II analyzer (MicrotracBEL). Prior to the measurement, the samples were degassed at $300 \text{ }^\circ\text{C}$ for 2 h in order to remove undesired surface adsorbates. The BET surface area was calculated using the adsorption data in the relative pressure range of 0 to 0.5.

Scanning electron microscopy (SEM) was employed to examine the surface morphology and distribution of the catalyst over the stagnation disk. The SEM images were obtained on a QuantaTM 250 FEG operated at an accelerating voltage of 20 kV.

Temperature-programmed reduction (TPR) was conducted to evaluate the reducibility of the catalyst, which may be influenced by an interaction between the nickel metal and the alumina support. The TPR experiments were performed using approximately 0.1 g of the powder catalyst, which were placed in a quartz glass reactor and heated from room temperature to $900 \text{ }^\circ\text{C}$ at a heating rate of $10 \text{ }^\circ\text{C min}^{-1}$ in a mixture of 10 % H_2 in Ar (50 mL min^{-1}). Simultaneously, the H_2 consumption was monitored by a thermal conductivity detector (TCD).

3 Reaction Kinetics

3.1 Kinetic Modeling Approach

In the DETCHEM^{STAG} [39] code, the mean field approximation approach is used to model the multistep surface reaction as described in earlier studies [23, 32]. Hence, the catalyst bed is described by means of coverages with adsorbed species, where there are no local variations in the stagnation flow configuration because of a radially uniform boundary layer. The state of the surface is described in terms of surface coverages θ_i . They can be converted into surface concentrations c_i by Eq. (13).

$$\theta_i = \frac{c_i \sigma_i}{\Gamma} \quad (13)$$

where σ_i is a number of occupied sites, and Γ is the surface site density. For nickel catalysts it was determined to a value of $\Gamma = 2.49 \cdot 10^{-9} \text{ mol cm}^{-2}$ [48].

The molar net production rates (\dot{s}_i) can be described in analogy to gas-phase reactions by

$$\dot{s}_i = \sum_{j=1}^{K_s} \nu_{ij} k_{fj} \prod_{i=1}^{N_g+N_s} c_i^{\nu'_{ij}} \quad (14)$$

Here, the mechanism consists of K_s surface reactions among N_g gas-phase species and N_s surface species; ν_{ij} denote the stoichiometric coefficients of reactants and products, whereas ν'_{ij} are reaction orders. For elementary-step reactions the latter ones are identical with the stoichiometric coefficients of the reactants. The temperature-dependent rate coefficients k_{fj} are written in the Arrhenius form (pre-exponential factor A_j , temperature exponent β_j , and activation energy E_{aj}) with an optional term to include coverage-dependent activation energies ε_{ij} and coverage-dependent reaction orders μ_{ij} .

$$k_{fj} = A_j T^{\beta_j} \exp\left(-\frac{E_{aj}}{RT}\right) \prod_{i=1}^{N_s} \theta_i^{\mu_{ij}} \exp\left(\frac{\varepsilon_{ij}\theta_i}{RT}\right) \quad (15)$$

$F_{\text{cat/geo}}$ is another parameter that needs to be calculated. It is the catalytically active surface area of the nanoparticles (A_{cat}) in relation to the reactor surface area (A_{geo}), i.e., the area of the circular plate; $d_{\text{nanoparticle}}$ is taken from literature [49, 50].

$$F_{\text{cat/geo}} = \frac{A_{\text{cat}}}{A_{\text{geo}}} \quad (16)$$

$$A_{\text{cat}} = \frac{m_{\text{cat}}}{\rho_{\text{cat}}} \frac{6}{d_{\text{nanoparticle}}} \quad (17)$$

The catalytic surface area can be calculated using measured particle diameters from characterization or data from literature [49, 50].

3.2 Surface Reaction Mechanism and Kinetics

A reliable microkinetic reaction mechanism should be independent of the reactor type and reaction conditions. Many investigations on the kinetics of ammonia decomposition have been accomplished recently. A review paper on ammonia decomposition covers the various kinetic models that have been used for various catalysts [37].

The major reaction pathways of ammonia decomposition are similar for the mechanisms proposed for different catalysts. They consist of three processes: ammonia adsorption,

stepwise dehydrogenation, and desorption of the reactants. The specific catalyst, however, might lead to different rate-determining steps [38].

With respect to the ammonia decomposition on nickel, Appari et al. [48] suggested a model with 22 reactions for use in modeling the thermocatalytic reactions on the electron-conducting material nickel inside the anode of a solid oxide fuel cell (SOFC). Because of the system, they recommended reactions for hydrogen oxidation along with ammonia deposition. On the other hand, Zhu et al. (2022) [51] proposed a set of 12 reactions for ceramic fuel cells containing nickel. Both models have been examined in our study. Using DETCHEM software [39], the models' repeatability and thermodynamic consistency were checked. The numerical simulation was conducted using DETCHEM and FLUENT [45] software, and the outcome was compared with experimental data using CaRMEn software [52, 53]. Figs. 6 and 7 depict the energy diagrams for the two implemented mechanisms. In more detail, Tab. 2 gives a list of the Appari et al. (2011) [48] and the Zhu et al. (2022) [51] nickel-based surface reaction mechanism of ammonia decomposition.

4 Results and Discussion

4.1 CFD Calculation of the Stagnation-Flow Reactor

The boundary conditions and numerical parameters for the 3D CFD calculation with the program FLUENT [45] are given in Sect. 2.2.1. The temperature of the wall of the disk was set to $T = 600 \text{ }^\circ\text{C}$ and the mechanism of Zhu et al. was utilized [51]. The FLUENT code does not offer a washcoat model.

Fig. 8 presents the velocity field depicted with streaklines (particle path lines). At the inlet the streaklines are parallel. Towards the plate these deviate more and more from the vertical direction and are deflected into radial direction. The flow turns around the circumferential edge of the disk

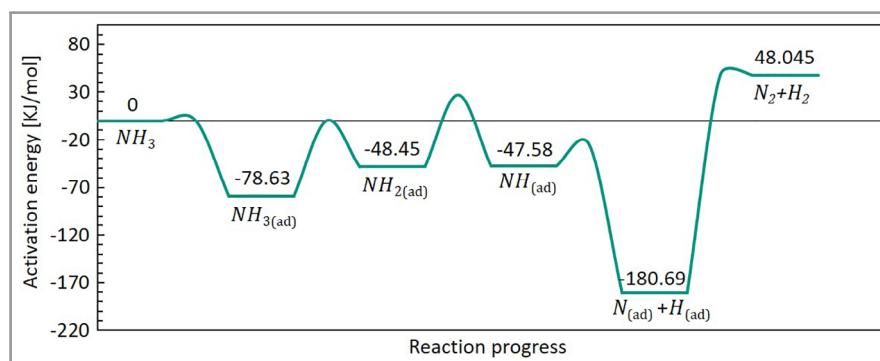


Figure 6. Energy diagram of the ammonia decomposition reaction over a Ni catalyst according to the mechanism by Appari et al. [48]. (ad) refers to adsorbed species.

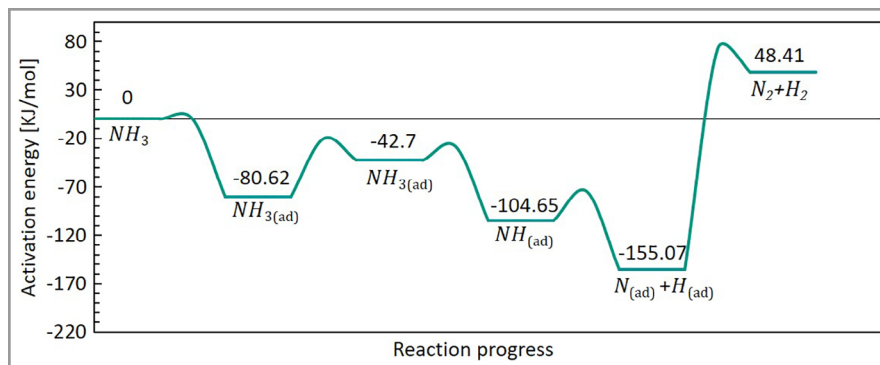


Figure 7. Energy diagram of the ammonia decomposition reaction over a Ni catalyst according to the mechanism by Zhu et al. [51]. (ad) refers to adsorbed species.

and turns back again to vertical direction to reach the circular orifice at the outlet. A recycling zone is established behind the closed part of the top end of the SFR. Moreover, the sketch presents an iso-surface (in green) where the axial velocity u_z in the system is zero.

To be more precise, Fig. 9 shows a 2D iso-plot of the axial velocity u_z together with some vector arrows in the z - r plane. The symmetry axis is on the right side and the z -coordinate points upwards. The axial velocity decreases towards the value zero on the plate surface. Two lines in the figure signify constant velocity. The iso-line of zero axial velocity $u_z = 0 \text{ m s}^{-1}$ separates the part of the recirculation zone where the flow moves upwards. The iso-line of velocity $u_z = 0.002 \text{ m s}^{-1}$ is near the disk surface and shows that the boundary layer of axial velocity exhibits a constant thickness for radial positions which are smaller than $r \approx 0.015 \text{ m}$.

around the symmetry axis, which leads to two highlights. Firstly, the modeling of the reactor with a 1D approach is sufficient. As a result, the experimental outcomes are comparable with numeric result of the 1D DETCHEM^{STAG} code. Secondly, the radial position for the probe to measure the axial profile of any quantity is not important as long as the radial position is smaller than $r \approx 0.015 \text{ m}$.

4.2 Catalyst Characterization

Fig. 12 depicts the X-ray diffraction pattern of the 20 wt % Ni/Al₂O₃ catalyst; reflexes at 37.2°, 45.6°, and 66.7° are attributed to Al₂O₃, whereas reflexes at 43.3°, 51.2°, and 79.4° suggest the presence of Ni crystallites [43, 54]. According to the N₂-physisorption data presented in Tab. 3, the addition of Ni to the Al₂O₃ support material changes the specific surface area as well as the pore volume. In particular, the

Table 2. Surface reaction mechanism of ammonia decomposition according to the models proposed by Appari et al. [48] and Zhu et al. [51]. (ad) refers to adsorbed species and the sticking coefficient is indicated by s .

	Reactant	Product	Zhu et al. [51]			Appari et al. [48]		
			A [cm, s]	β	E [kJ mol ⁻¹]	A [cm, s]	β	E [kJ mol ⁻¹]
1	N ₂ + 2 Ni _(ad)	2 N _(ad)	1.38×10^{-06s}	0	47.882	1.000×10^{-06s}	0	0
2	2 N _(ad)	2 Ni _(ad) + N ₂	$2.17 \times 10^{+16}$	-0.126	120.248	$4.442 \times 10^{+22}$	0	210.84
3	H ₂ + 2 Ni _(ad)	2 H _(ad)	1.97×10^{-03s}	0	0	1.000×10^{-02s}	0	0
4	2H _(ad)	2 Ni _(ad) + H ₂	$5.66 \times 10^{+20}$	-0.117	111.529	$3.315 \times 10^{+19}$	0	82.21
5	NH ₃ + Ni _(ad)	NH _{3(ad)}	1.90×10^{-05s}	-0.097	0.02	1.100×10^{-02s}	0	0
6	NH _{3(ad)}	Ni _(ad) + NH ₃	$5.79 \times 10^{+11}$	-0.161	80.642	$8.210 \times 10^{+14}$	0	78.63
7	H _(ad) + N _(ad)	NH _(ad) + Ni _(ad)	$7.00 \times 10^{+20}$	-0.161	80.4	$2.070 \times 10^{+19}$	0	156.04
8	NH _(ad) + Ni _(ad)	N _(ad) + H _(ad)	$6.18 \times 10^{+19}$	-0.161	29.984	$6.213 \times 10^{+19}$	0	22.93
9	NH _(ad) + H _(ad)	NH _{2(ad)} + Ni _(ad)	$7.72 \times 10^{+19}$	-0.161	76.478	$3.702 \times 10^{+19}$	0	74.87
10	NH _{2(ad)} + Ni _(ad)	NH _(ad) + H _(ad)	$5.33 \times 10^{+19}$	-0.161	14.525	$2.718 \times 10^{+22}$	0	75.74
11	NH _{2(ad)} + H _(ad)	Ni _(ad) + NH _{3(ad)}	$6.06 \times 10^{+19}$	-0.161	22.278	$1.320 \times 10^{+24}$	0	48.81
12	NH _{3(ad)} + Ni _(ad)	NH _{2(ad)} + H _(ad)	$1.78 \times 10^{+20}$	-0.161	60.2	$5.723 \times 10^{+22}$	0	78.99

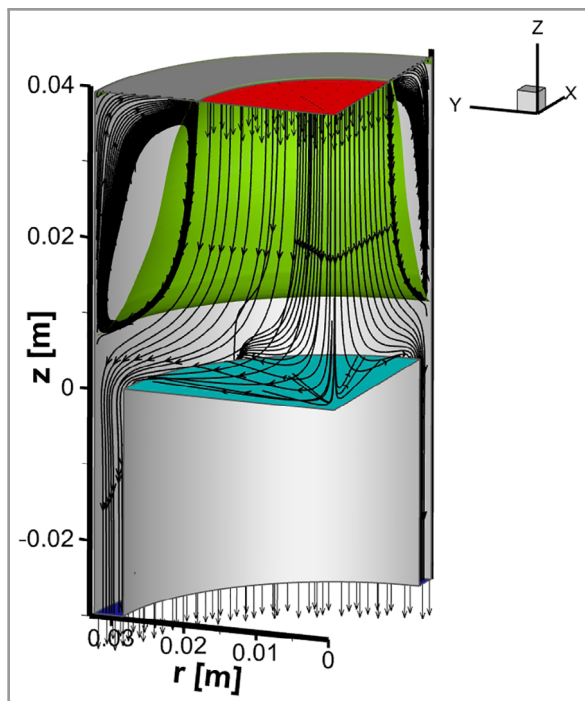


Figure 8. Qualitative velocity field inside the SFR.

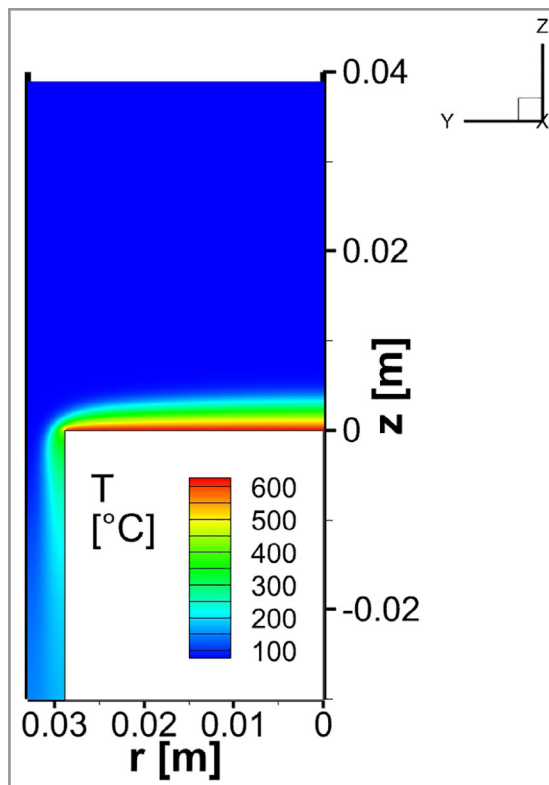


Figure 10. Iso-plot of temperature T in z - r plane.

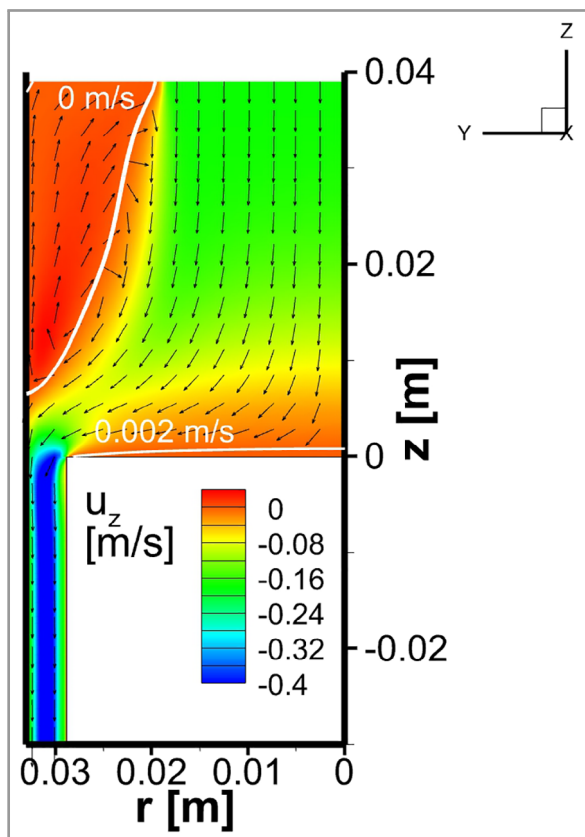


Figure 9. Iso-plot of axial velocity u_z together with velocity vectors and two isolines for $u_z = 0/0.002 \text{ m s}^{-1}$ in z - r plane.

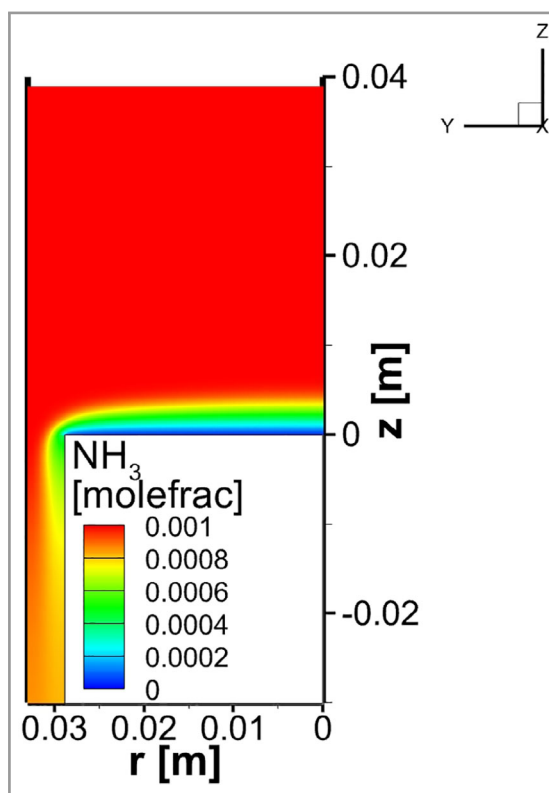


Figure 11. Iso-plot of the NH_3 mole fraction in z - r plane.

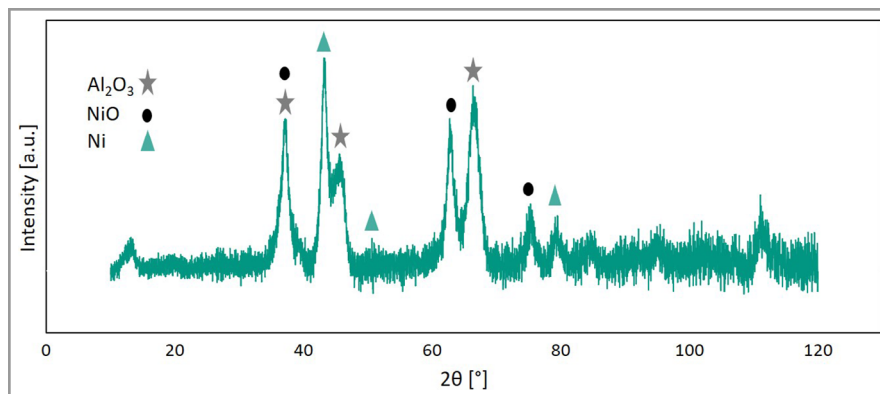


Figure 12. XRD pattern of the 20 wt % Ni/Al₂O₃ catalyst.

Table 3. Summary of the results from N₂-physisorption measurements (evaluated according to the BET method) for Al₂O₃ and 20 wt % Ni/Al₂O₃.

Parameter	Al ₂ O ₃	20 wt % Ni/Al ₂ O ₃
V_m [cm ³ (STP)g ⁻¹]	32.24	36.60
$a_{s,BET}$ [m ² g ⁻¹]	140	159
d_p [nm]	26.6	8.5
V_p [cm ³ g ⁻¹]	0.95	0.37
a_p [m ² g ⁻¹]	166	211

specific surface area, V_m , of Al₂O₃ (140 m²g⁻¹) increases to 159 m²g⁻¹ upon Ni addition. Furthermore, the Barrett-Joyner-Halenda (BJH) method was employed to calculate the average pore width and pore volume from the desorption branch of the isotherm. As indicated in Tab. 3, the addition of Ni to alumina causes a decrease of both the pore diameter d_p (from 26.6 to 8.5 nm) and the pore volume V_p (from 0.95 to 0.37 cm³g⁻¹).

SEM characterization of the as-prepared washcoated stagnation disk (Fig. 13a) confirms that the catalyst was evenly distributed across the disk's surface, which is crucial for a smooth and uniform SFR solid surface. The figure is a clear

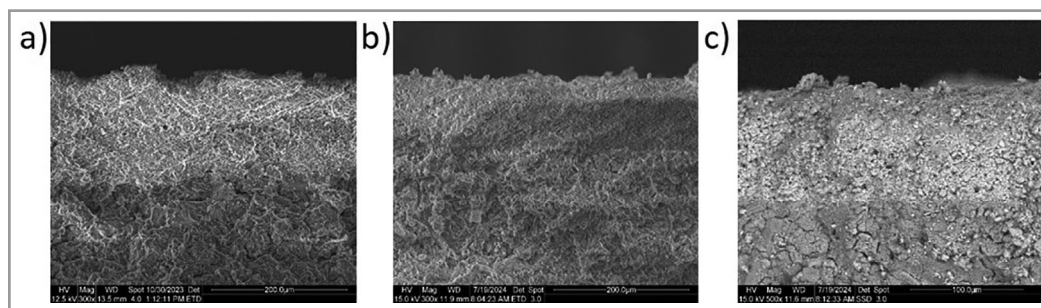


Figure 13. SEM images of the 20 wt % Ni/Al₂O₃ catalyst. a) Fresh catalyst (image obtained from secondary electron (SE) measurements); b) spent catalyst (image obtained from SE measurements); c) spent catalyst (image obtained from backscattered electron (BSE) measurements).

assessment of the coating method and the resulting distribution. In order to determine the structural stability of the washcoat under reactive conditions, Figs. 13b and 13c display a spent catalyst that was used for NH₃ decomposition experiments. According to the SEM images, pronounced morphological changes of the washcoat structure do not occur on the micrometer scale.

Furthermore, the TPR profile of the 20 wt % Ni/Al₂O₃ catalyst depicted in Fig. 14 reveals reduction peaks that match well with those reported in previous studies on NiO supported on alumina [43, 55, 56]: reduction peaks in the temperature range of 300–500 °C can be attributed to the reduction of surface NiO, whereas peaks in the range of 450–650 °C originate from the reduction of bulk NiO. In the TPR profile obtained for the 20 wt % Ni/Al₂O₃ catalyst studied herein, the initial peak that corresponds to the reduction of surface NiO species, which generally occurs at lower temperatures compared to bulk NiO due to weaker metal-support interactions, is found at around 350 °C. The reduction of bulk NiO species, which requires higher temperatures due to stronger metal-support interactions, causes a second peak at approx. 550 °C. The subsequent decrease in TCD signal intensity upon further temperature increase indicates that the majority of NiO has been reduced to metallic nickel (Fig. 14). Notably, the reduction of the Al₂O₃ support would require even higher temperatures.

4.3 Measurements and Calculations of Species Profiles

The activity of the 20 wt % Ni/Al₂O₃ catalyst for ammonia decomposition has been investigated in the SFR under various operating conditions. Since diverse pretreatment methods lead to different catalyst behaviors, the duration

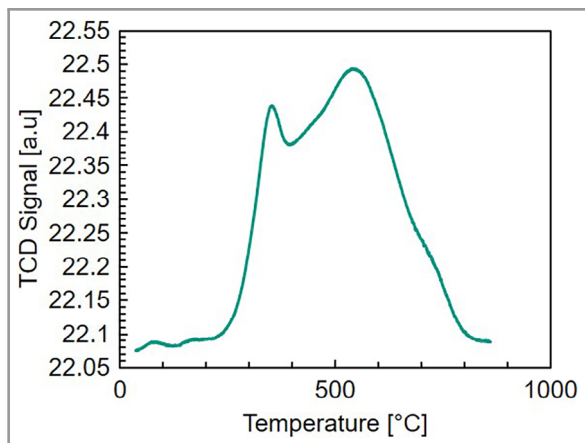


Figure 14. TPR profile of the 20 wt % Ni/Al₂O₃ catalyst during heating with 10 °C min⁻¹ in a mixture of 10 % H₂ in Ar.

of the treatment was varied before a measurement was performed to evaluate the effect of the pretreatment on the catalytic performance in our system. Preliminary research suggests that hydrogen reduction is necessary for the catalyst to become active before the test [57–59]. In 2004, Ganley et al. [60] compared several catalyst metals on alumina supports and oxidized them for 480 min at 550 °C before the catalyst was reduced. In our present work, the reactor was fed with 10 % O₂ in balance N₂ at a flow rate of 5 L min⁻¹, 600 °C, and 900 mbar. Afterwards, hydrogen was introduced under the same conditions for the same duration. The catalyst was flushed using pure nitrogen under the same operating conditions after each stage was completed. Single-stage pretreatment duration ranged from 15, 30, 60, to 90 min. Following each of the four pretreatment protocols, the reactor was cooled, and a light-off test was performed using a ramp rate of 3 °C min⁻¹ between 300 °C and 500 °C to evaluate the catalytic activity post-pretreatment. This was carried out by feeding 1000 ppm ammonia in balance Ar into the reactor at a flow rate of 10 L min⁻¹, placing the sampling probe 0.5 mm from the surface and using the mass spectrometer to sample at a rate of 1 Hz.

The light-off results depicted in Fig. 15 demonstrate how varying the time (the time here refers to the duration of a single step in the pretreatment) results in different ammonia conversion rates, i.e., the measured outlet NH₃ molar fraction. Given that the 30-min pretreatment demonstrated the highest conversion in the tested temperature range, a second measurement under the same conditions was repeated to ensure its

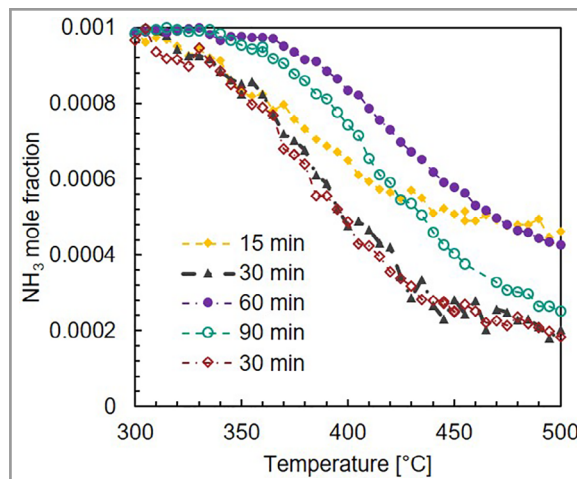


Figure 15. Light-off of ammonia decomposition measurements with different pretreatment durations (15, 30, 60, and 90 min) over 20 wt % Ni/Al₂O₃ ($p = 900$ mbar, NH₃ inlet mole fraction = 0.001, balance Ar, flow rate = 10 L min⁻¹, distance from surface = 0.5 mm). That the last curve is congruent with the second curve (30 min) confirms the reproducibility of the data.

reproducibility, as evidenced by the final curve in Fig. 15. The outcome of the measurement leads to choosing the 30-min procedure as the pretreatment protocol for all measurements discussed in the following.

Fig. 16 presents the resulting concentration profiles of three varying light-off tests performed at three different pressures, namely, 600, 900, and 1200 mbar, with all other parameters remaining constant. In each case, the reactor feed consisted of 10 L min⁻¹ of 1000 ppm NH₃ balanced in Ar, the probe was positioned 0.5 mm from the surface, and the temperature was increased at a ramp rate of 3 °C min⁻¹ up to 550 °C. Fig. 16 also includes the simulation results from the reaction mechanisms of Zhu et al. [51] and

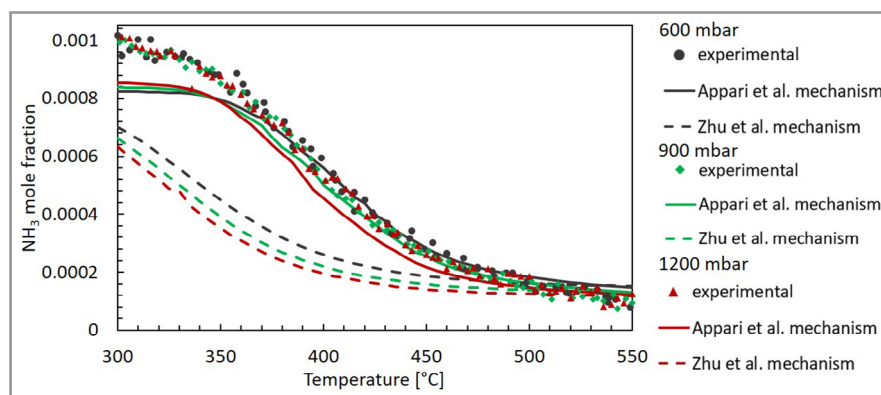


Figure 16. Comparison of experimental light-off data (symbols) for pressures of 600, 900, and 1200 mbar with numerical simulation results (lines) applying Zhu et al. [51] and Appari et al. [48] mechanisms (NH₃ inlet mole fraction = 0.001, balance Ar, flow rate = 10 L min⁻¹, distance from surface = 0.5 mm).

Appari et al. [48] to perform a comparison between the experimental data and the simulation. Considering the approximately 5-min delay between the mass spectrometer signal and the catalytic surface temperature signal, which may result in a thermocouple temperature offset of +15 K, the experimental profiles in the figure have been corrected to enable a consistent comparison with the simulated results.

The three curves of experimental results are congruent, indicating that minor pressure changes do not significantly affect the decomposition reaction. Irrespective of the pressure chosen, the reaction starts at approx. 300 °C, and the mole fraction of ammonia decreases with increasing temperature from the value of 0.001 to around 0.00009 at ca. 550 °C, which corresponds to an ammonia conversion of 90 %. As it is evident in the graph, the results using the mechanism by Appari et al. [48] show a better agreement with the experimental data. It is important to note that different catalyst systems were used for the development of the two mechanisms.

The mechanism of Appari et al. [48] was initially developed without taking into account any support effects and was developed on the basis of experimental data over Ni/SiO₂. Contrary, the mechanism proposed by Zhu et al. [51] is to model experimental data with a Ni-BCZYb catalyst validated by experiments performed on Ni/BaZrO₃. In this study, it has been considered that the contribution of Al₂O₃ to the catalytic NH₃ decomposition process is negligible, which makes it an inert support for the reactions and therefore may justify the better performance of the mechanism of Appari et al. [48] with respect to the experimental data in Fig. 16. At higher temperatures, however, because of the high conversion, the reaction is controlled by the diffusion limitations rather than kinetics; therefore, it is anticipated that both mechanisms exhibit good agreement.

To further understand the differences between the outcomes of the two mechanisms employed in Fig. 16, the temperature-dependent surface coverages are shown in Fig. 17 for the Ni vacancies (left graph) and atoms of nitrogen adsorbed on Ni (right graph) for the reaction mechanisms of Zhu et al. [51] and Appari et al. [48]. In agreement with literature [37, 38], the surface is predominantly occupied by nitrogen species (N), with the desorption of N₂ being the rate-limiting step. As the temperature increases, desorption of nitrogen species is promoted, resulting in more free nickel (Ni) sites. The number of free sites is the key indicator for the global reaction rate. Despite the same trends in the graphs of the Ni coverage for both mechanisms (Fig. 17), Zhu et al. [51] predict a lower quantity of empty sites than the other one. This becomes signifi-

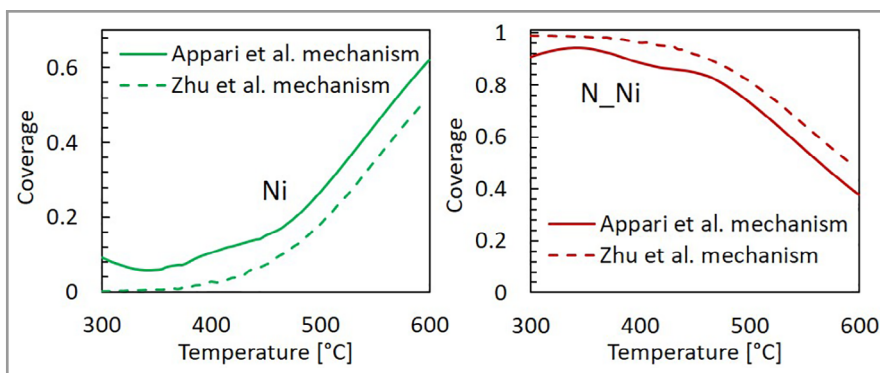


Figure 17. Comparison of Ni coverage (left graph) and N_{Ni} coverage (right graph) as a function of temperature calculated using two detailed reaction mechanisms by Zhu et al. [51] and Appari et al. [48]. (NH₃ mole fraction = 0.001, balance Ar, $p = 900$ mbar, flow rate = 10 L min⁻¹, distance from surface = 0.5 mm).

cant for temperatures below 400 °C, where the availability of empty sites is considerably smaller than for the Appari et al. [48] mechanism. Therefore, we observe a deviation in the predictions of the two mechanisms for lower temperatures.

At this point, spatially resolved experimental results obtained at different pressures and different ammonia inlet mole fractions are compared with the results of the 1D calculations using the reaction mechanisms of Zhu et al. [51] and Appari et al. [48]. The surface temperature was set to 600 °C with a total flow rate of 10 L min⁻¹.

In Fig. 18 the mole fraction of ammonia is plotted against the distance over the surface (z -coordinate) for four different pressures (600, 900, 1050, and 1200 mbar). Regarding the thickness of the boundary layer of NH₃ concentration, a change in pressure has no significant impact, neither in the experiments nor in the simulations. The thickness of the ammonia boundary layer is about 7 mm in all cases. The experimental data exhibit small deviations of the gradient of the concentration profiles. However, since these deviations are not directly correlated to the pressure, they may rather be explained by uncertainties in quantification. The independency of the thickness of the boundary layer from pressure is predicted also in the 1D simulations, where the flow field depends only on the Reynolds number (Eq. (11)). Since during the experiments the mass flow rate (kg s⁻¹) was held constant for all pressures, the velocity is inversely proportional to the pressure; the same holds for the kinematic viscosity. Hence, the Reynolds number (around 520) was constant throughout the experiments. As a result, the thickness of the velocity boundary layer is also expected to be constant. The same accounts for the thickness of the concentration boundary [47].

Fig. 19 presents the experimental results obtained when varying the ammonia mole fraction in the feed and compares them with simulations conducted by using the two mechanisms published by Zhu et al. [51] and Appari et al. [48]. Apart from the NH₃ content in the feed gas stream, all other conditions were kept constant, i.e., a total flow rate of

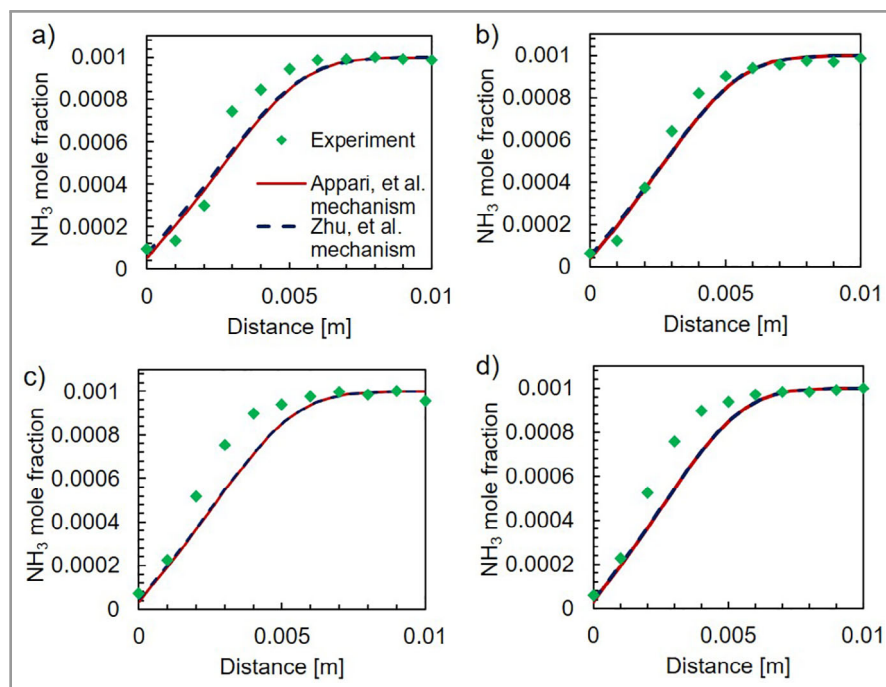


Figure 18. Comparison of experiment and simulation data of ammonia mole fractions as a function of the z-coordinate (distance of microprobe from the catalyst surface) for two reaction mechanisms by Zhu et al. [51] and Appari et al. [48] (NH₃ inlet mole fraction = 0.001, balance Ar, flow rate = 10 L min⁻¹, T = 600 °C). Pressure in mbar: a) 600, b) 900, c) 1050, d) 1200.

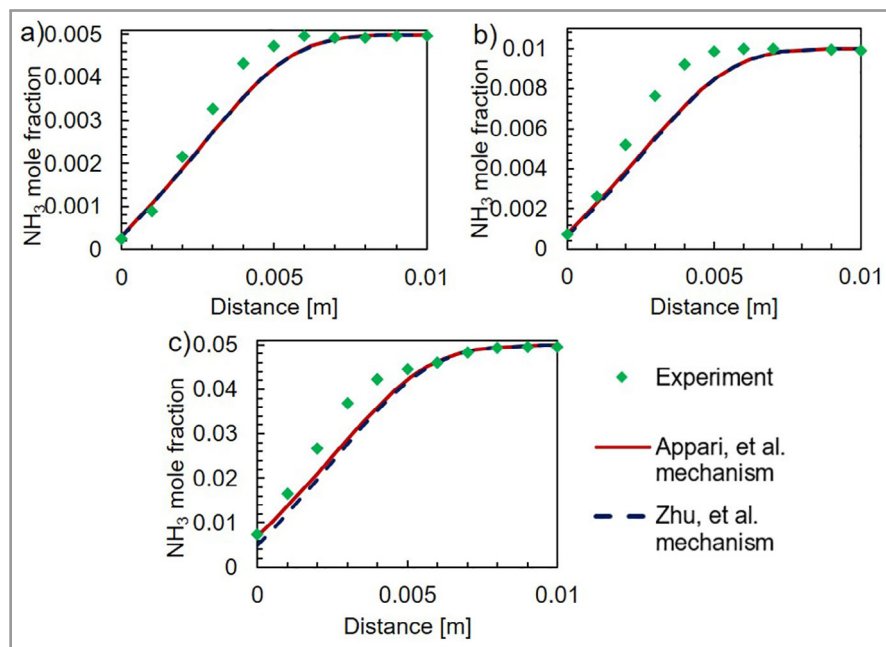


Figure 19. Comparison of experiment and simulation data of ammonia mole fractions as a function of the z-coordinate (distance of microprobe from the catalyst surface) for two reaction mechanisms from Zhu et al. [51] and Appari et al. [48] (flow rate = 10 L min⁻¹, p = 900 mbar, T = 600 °C, balance Ar). Ammonia inlet in mole fractions [-]: a) 0.005, b) 0.01, c) 0.05.

10 L min⁻¹, a pressure of 900 mbar, and a surface temperature of 600 °C. By increasing the ammonia concentration in the feed, the concentration near the surface rises. This shows that the system is more and more kinetically-controlled. Due to the finite surface reaction rate it is not possible to convert all the ammonia at the surface for a larger inlet concentration. If the process would be diffusion-controlled, then the NH₃ decomposition rate would be large enough to guarantee an ammonia concentration of zero on the catalyst surface.

As already demonstrated for low temperatures, it can be seen that for the largest inlet concentration (towards diffusion-controlled systems) the mechanism of Appari et al. [48] predicts a smaller conversion than the mechanism of Zhu et al. [51], which fits better with experimental data. However, the thickness of the NH₃ boundary layer remains constant. According to the experimental data, a conversion of 95 % can be achieved on the surface if an inlet mole fraction of 0.001 is chosen. The conversion on the surface drops to 85 % when the ammonia feed concentration is increased to a mole fraction of 0.05. The simulations match fairly well and deviate only slightly. For a concentration of 1000 ppm NH₃ in the feed (mole fraction of 0.001), the mechanisms by Appari et al. [48] and Zhu et al. [51] predict a surface ammonia molar fraction of 38.4×10^{-6} and 50.6×10^{-6} , respectively, which corresponds to a conversion rate of 96 % and 95 %, respectively. By raising the NH₃ feed gas concentration to 50 000 ppm, the conversion rates decline to 86 % and 90 %, accordingly.

Based on these results, it is evident that the 1D flow model is able to describe the interaction of convection, diffusion, and reaction very well for both detailed kinetic models used. This holds for operational conditions that guarantee a

diffusion-controlled system (large temperature or large inlet concentration).

5 Conclusion

Experimental and numerical investigations on the decomposition of ammonia over a nickel-based catalyst in a stagnation-flow reactor are presented. This unique reactor geometry ensures conditions where physical parameters are only dependent on the distance from the stagnation disk (1D dependency). Exploiting this feature, profiles of temperature and concentrations have been obtained experimentally using a microprobe technique for different pressures and NH_3 feed concentrations.

Additionally, the flow field and species distribution inside the reactor have been numerically calculated using a 3D CFD code. The calculations underscore the stagnation point flow design of the reactor and confirm the one-dimensionality in the actual setup. Therefore, experimental data can be simulated with a numerical program solving the equations of a 1D model for stagnation flows.

The experimental results uncovered that the light-off and the concentration profiles during NH_3 decomposition are barely dependent on the pressure in the range of 600–1200 mbar. The agreement to the 1D calculation is good at higher temperatures for two detailed reaction mechanisms that were previously suggested in literature for describing Ni-catalyzed NH_3 decomposition. At 600 °C the differences between the results of both detailed reaction mechanisms are negligible. The thickness of the NH_3 concentration boundary layer was found to be about 7 mm, and the conversion of ammonia on the surface is approximately 95 % both for experimental and numerical data.

Increasing the inlet concentration of ammonia from 1000 to 50000 ppm leads to an increase in concentration of ammonia near the surface and shifts the system from a diffusion-controlled towards a kinetically influenced regime. It should be noted that both mechanisms request evaluation at conditions that lead to lower conversion. Also, in this case, the analysis of experiments and mechanisms reveals a good alignment for varied ammonia concentrations at the feed. However, the system changed from being diffusion-controlled to being kinetically-controlled for lower temperatures. This regime highlights the distinctions between the two mechanisms. Compared to Zhu et al. [51], the mechanism of Appari et al. [48] exhibits a significantly higher degree of agreement for the light-off curves. It is important to remember that the two systems were developed and validated using different support materials.

The findings promote the stagnation-flow reactor equipped with a moving capillary for taking samples as a useful setup for studying the surface kinetics of heterogeneously catalyzed gas-phase reactions. It permits a relatively simple data gathering process and substantially decreases the time needed for modeling because a comparably simple

1D approach of the transport equations can be applied. Furthermore, the results confirm that the nickel catalyst used is a promising alternative to more expensive metals.

Acknowledgment

A cost-free academic license of DETCHEM™ and CaRMeN by omegadot software & consulting GmbH, Limburgerhof, Germany, is gratefully acknowledged. Furthermore, we acknowledge Andrea De Giacinto and Kathrin Schäfer (ITCP, KIT) for support regarding N_2 -physisorption measurements, Lukas Braun (ITCP, KIT) for assistance regarding XRD measurements, Philipp Blanck (ITCP, KIT) for performing the SEM analysis, finally, Thomas J. Eldridge and Angela Deutsch for conducting the BET characterization. We would like to thank R. J. Kee for collaboration and very fruitful discussions. This work was funded by the Deutsche Forschungsgemeinschaft (DFG, German Research Foundation) through projects SFB 1441 – Project-ID 426888090, and Project NSF-DFG Echem, Project-ID 460038541.

Open access funding enabled and organized by Projekt DEAL.

Symbols used

a	[mol m ⁻³]	activity
A_j	[mol, m, s]	pre-exponential factor
a_p	[m ² g ⁻¹]	catalyst pore area
$a_{s,BET}$	[m ² g ⁻¹]	specific surface area
c_i	[mol L ⁻¹]	concentration
D	[m]	diameter
$D_{i,M}$	[m ² s ⁻¹]	averaged diffusion coefficient
d_p	[nm]	catalyst pore diameter
E_a	[J mol ⁻¹]	activation energy
\hat{j}_i	[mol m ⁻² s ⁻¹]	molar diffusion flux
k	[s ⁻¹]	rate constant
L	[m]	distance between the inlet and disk
M	[g mol ⁻¹]	molecular mass
\bar{M}	[g mol ⁻¹]	averaged molecular mass
N	[-]	number of species
p	[mbar, atm, bar]	pressure
R	[J mol ⁻¹ K ⁻¹]	gas constant
Re	[-]	Reynolds number
\dot{s}	[mol m ⁻² s ⁻²]	surface reaction rate
T	[°C]	temperature
u	[m s ⁻¹]	Stefan velocity
V	[m s ⁻¹]	scaled radial velocity
V_p	[cm ³ g ⁻¹]	catalyst pore volume
X_i	[-]	mole fraction in gas phase
Y_i	[-]	mass fraction in gas phase
z	[m]	axial coordinate

Greek letters

β	[-]	extended Arrhenius parameter
Γ	[mol m ⁻²]	surface site density
Δx^+	[m]	width
ΔH^{298K}	[kJ mol ⁻¹]	reaction standard enthalpy
δ	[m]	boundary layer thickness
ε	[-]	porosity
η	[-]	effectiveness factor
θ_i	[-]	coverage
Λ	[-]	eigenvalue of the radial momentum equation
μ	[Ns m ⁻²]	viscosity
ν	[m ² s ⁻¹]	kinematic viscosity
v_x	[m s ⁻¹]	axial velocity
ρ	[g m ⁻³]	density
σ	[-]	number of occupied adsorption sites per adsorbed molecule
ν'_{ij}	[-]	stoichiometric coefficient
$\dot{\omega}$	[mol s ⁻¹]	gas phase reaction rate

Abbreviations

BCZY	yttrium- and ceria-doped barium zirconate
BET	Brunauer-Emmett-Teller
BJH	Barrett-Joyner-Halenda
BSE	backscattered electron
CFD	computational fluid dynamics
CVD	chemical vapor decomposition
MS	mass spectrometry
PBR	packed-bed reactor
SE	secondary electron
SEM	scanning electron microscopy
SFR	stagnation-flow reactor
SOFC	solid oxide fuel cell
TCD	thermal conductivity detector
TPR	temperature-programmed reduction
VOCs	volatile organic compounds
XRD	X-ray diffraction

References

- [1] C. Karakaya, O. Deutschmann, *Chem. Eng. Sci.* **2013**, *89*, 171–184. DOI: <https://doi.org/10.1016/j.ces.2012.11.004>
- [2] R. Kee, F. Rupley, J. Miller, *Chemkin-II: A Fortran Chemical Kinetics Package for the Analysis of Gas-Phase Chemical Kinetics* **1989**.
- [3] R. J. Kee, J. A. Miller, G. H. Evans, G. Dixon-Lewis, *Symp. (Int.) Combust.* **1989**, *22* (1), 1479–1494. DOI: [https://doi.org/10.1016/S0082-0784\(89\)80158-4](https://doi.org/10.1016/S0082-0784(89)80158-4)
- [4] *Fundamentals of Heat and Mass Transfer*, 8th ed. (Eds.: T. L. Bergman, A. Lavine, F. P. Incropera), John Wiley & Sons, Hoboken, NJ **2019**.
- [5] R. J. Kee, *PREMIX: A Fortran Program for Modeling Steady Laminar One-Dimensional Premixed Flames* **1998**.
- [6] A. H. Dilawari, J. Szekely, *J. Cryst. Growth* **1991**, *108* (3–4), 491–498. DOI: [https://doi.org/10.1016/0022-0248\(91\)90226-U](https://doi.org/10.1016/0022-0248(91)90226-U)
- [7] P. N. Gadgil, *J. Cryst. Growth* **1993**, *134* (3–4), 302–312. DOI: [https://doi.org/10.1016/0022-0248\(93\)90140-R](https://doi.org/10.1016/0022-0248(93)90140-R)
- [8] G. Luo, S. P. Vanka, N. Glumac, *Int. J. Heat Mass Transfer* **2004**, *47* (23), 4979–4994. DOI: <https://doi.org/10.1016/j.ijheatmasstransfer.2004.06.012>
- [9] K. Swain, B. Mahanthesh, F. Mebarek-Oudina, *Heat Transfer* **2021**, *50* (1), 754–767. DOI: <https://doi.org/10.1002/htj.21902>
- [10] J. C. Misra, A. Sinha, B. Mallick, *Physica A* **2017**, *470*, 330–344. DOI: <https://doi.org/10.1016/j.physa.2016.10.051>
- [11] L. L. Raja, R. J. Kee, R. Serban, L. R. Petzold, *J. Electrochem. Soc.* **2000**, *147* (7), 2718. DOI: <https://doi.org/10.1149/1.1393595>
- [12] S. S. Ghadikolaie, M. Yassari, H. Sadeghi, K. Hosseinzadeh, D. D. Ganji, *Powder Technol.* **2017**, *322*, 428–438. DOI: <https://doi.org/10.1016/j.powtec.2017.09.006>
- [13] R. Lam, D. G. Vlachos, *Phys. Rev. B* **2001**, *64* (3), 035401. DOI: <https://doi.org/10.1103/PhysRevB.64.035401>
- [14] J. Li, H. G. Im, *Combust. Flame* **2006**, *145* (1–2), 390–400. DOI: <https://doi.org/10.1016/j.combustflame.2005.08.041>
- [15] T. Yuan, Y.-H. Lai, C.-K. Chang, *Combust. Flame* **2008**, *154* (3), 557–568. DOI: <https://doi.org/10.1016/j.combustflame.2008.06.005>
- [16] G. D. Wehinger, T. Eppinger, M. Kraume, *Chem. Eng. Sci.* **2014**, *III*, 220–230. DOI: <https://doi.org/10.1016/j.ces.2014.02.025>
- [17] E. Meeks, R. J. Kee, D. S. Dandy, M. E. Coltrin, *Combust. Flame* **1993**, *92* (1–2), 144–160. DOI: [https://doi.org/10.1016/0010-2180\(93\)90204-G](https://doi.org/10.1016/0010-2180(93)90204-G)
- [18] F. Montecchio, H. Persson, K. Engvall, J. Delin, R. Lanza, *Chem. Eng. J.* **2016**, *306*, 734–744. DOI: <https://doi.org/10.1016/j.cej.2016.07.117>
- [19] J. Warnatz, M. D. Allendorf, R. J. Kee, M. E. Coltrin, *Combust. Flame* **1994**, *96* (4), 393–406. DOI: [https://doi.org/10.1016/0010-2180\(94\)90107-4](https://doi.org/10.1016/0010-2180(94)90107-4)
- [20] H. Karadeniz, C. Karakaya, S. Tischer, O. Deutschmann, *Chem. Eng. Sci.* **2013**, *104*, 899–907. DOI: <https://doi.org/10.1016/j.ces.2013.09.038>
- [21] R. J. Kee, W. Yang, L. L. Raja, C. A. Wolden, *Proc. Combust. Inst.* **2000**, *28* (1), 1381–1388. DOI: [https://doi.org/10.1016/S0082-0784\(00\)80353-7](https://doi.org/10.1016/S0082-0784(00)80353-7)
- [22] J. D. Taylor, M. D. Allendorf, A. H. McDaniel, S. F. Rice, *Ind. Eng. Chem. Res.* **2003**, *42* (25), 6559–6566. DOI: <https://doi.org/10.1021/ie020934r>
- [23] C. Karakaya, H. Karadeniz, L. Maier, O. Deutschmann, *Chem-CatChem* **2017**, *9* (4), 685–695. DOI: <https://doi.org/10.1002/cctc.201601237>
- [24] G. D. Wehinger, Particle-Resolved CFD Simulations of Catalytic Flow Reactors / Partikel-Aufgelöste CFD-Simulationen von Katalytischen Strömungsreaktoren, *Thesis*, Technische Universität Berlin **2016**.
- [25] N. E. McGuire, N. P. Sullivan, O. Deutschmann, H. Zhu, R. J. Kee, *Appl. Catal., A* **2011**, *394* (1–2), 257–265. DOI: <https://doi.org/10.1016/j.apcata.2011.01.009>
- [26] D. W. Hahn, C. F. Edwards, K. F. McCarty, R. J. Kee, *Appl. Phys. Lett.* **1996**, *68* (15), 2158–2160. DOI: <https://doi.org/10.1063/1.116014>
- [27] I. Kim, D.-G. Chang, P. D. Dapkus, *J. Cryst. Growth* **1998**, *195* (1–4), 138–143. DOI: [https://doi.org/10.1016/S0022-0248\(98\)00585-5](https://doi.org/10.1016/S0022-0248(98)00585-5)
- [28] Y. Chae, W. G. Houf, A. H. McDaniel, J. Troup, M. D. Allendorf, *J. Electrochem. Soc.* **2004**, *151* (8), C527. DOI: <https://doi.org/10.1149/1.1760993>

- [29] S. F. Rice, A. H. McDaniel, E. S. Hecht, A. J. J. Hardy, *Ind. Eng. Chem. Res.* **2007**, *46* (4), 1114–1119. DOI: <https://doi.org/10.1021/ie060892x>
- [30] N. E. McGuire, N. P. Sullivan, R. J. Kee, H. Zhu, J. A. Nabity, J. R. Engel, D. T. Wickham, M. J. Kaufman, *Chem. Eng. Sci.* **2009**, *64* (24), 5231–5239. DOI: <https://doi.org/10.1016/j.ces.2009.08.030>
- [31] C. Karakaya, L. Maier, O. Deutschmann, *Int. J. Chem. Kinet.* **2016**, *48* (3), 144–160. DOI: <https://doi.org/10.1002/kin.20980>
- [32] O. Deutschmann, *Modeling and Simulation of Heterogeneous Catalytic Reactions: From the Molecular Process to the Technical System*, 1st ed., Wiley, New York **2011**.
- [33] O. Deutschmann, F. Behrendt, J. Warnatz, *Catalysis Today* **1994**, *21*, 461–470. DOI: [https://doi.org/10.1016/0920-5861\(94\)80168-1](https://doi.org/10.1016/0920-5861(94)80168-1)
- [34] O. Deutschmann, R. Schmidt, F. Behrendt, J. Warnatz, *Symp. (Int.) Combust.* **1996**, *26* (1), 1747–1754. DOI: [https://doi.org/10.1016/S0082-0784\(96\)80400-0](https://doi.org/10.1016/S0082-0784(96)80400-0)
- [35] F. Behrendt, O. Deutschmann, B. Ruf, J. Warnatz, *J. Vacuum Sci. Technol. A* **1996**, *14* (3), 1604–1608. DOI: <https://doi.org/10.1116/1.580304>
- [36] X. Duan, X. Zhou, D. Chen, in *Catalysis* (Eds: J. J. Spivey, K. M. Dooley, Y.-F. Han, K. M. Dooley), 1st ed., The Royal Society of Chemistry, London **2013**.
- [37] I. Lucentini, X. Garcia, X. Vendrell, J. Llorca, *Ind. Eng. Chem. Res.* **2021**, *60* (51), 18560–18611. DOI: <https://doi.org/10.1021/acs.iecr.1c00843>
- [38] S. Mateti, L. Saranya, G. Sathikumar, Q. Cai, Y. Yao, Y. (Ian) Chen, *Nanotechnology* **2022**, *33* (22), 222001. DOI: <https://doi.org/10.1088/1361-6528/ac55d1>
- [39] S. Tischer, A. Shirsath, E. Daymo, et al., DETCHEM software package, 2.9 ed., www.detchem.com, Karlsruhe **2022**.
- [40] S. Ristig, M. Poschmann, J. Folke, O. Gómez-Cápiro, Z. Chen, N. Sanchez-Bastardo, R. Schlögl, S. Heumann, H. Ruland, *Chem. Ing. Tech.* **2022**, *94* (10), 1413–1425. DOI: <https://doi.org/10.1002/cite.202200003>
- [41] F. Schüth, R. Palkovits, R. Schlögl, D. S. Su, *Energy Environ. Sci.* **2012**, *5* (4), 6278–6289. DOI: <https://doi.org/10.1039/C2EE02865D>
- [42] H. Muroyama, C. Saburi, T. Matsui, K. Eguchi, *Appl. Catal., A* **2012**, *443–444*, 119–124. DOI: <https://doi.org/10.1016/j.apcata.2012.07.031>
- [43] M. Andache, M. Rezaei, Z. Taherkhani, *Res. Chem. Intermed.* **2021**, *47* (9), 3661–3672. DOI: <https://doi.org/10.1007/s11164-021-04493-9>
- [44] C. Karakaya, R. Otterstätter, L. Maier, O. Deutschmann, *Appl. Catal., A* **2014**, *470*, 31–44. DOI: <https://doi.org/10.1016/j.apcata.2013.10.030>
- [45] ANSYS Fluent 2021 R2, available at <https://www.ansys.com/academic>.
- [46] H. Karadeniz, C. Karakaya, S. Tischer, O. Deutschmann, *Chem. Eng. Sci.* **2013**, *104*, 899–907. DOI: <https://doi.org/10.1016/j.ces.2013.09.038>
- [47] *Chemically Reacting Flow: Theory, Modeling, and Simulation*, 1st ed. (Eds.: R. J. Kee, M. E. Coltrin, P. Glarborg, H. Zhu), Wiley, New York **2017**.
- [48] S. Appari, V. M. Janardhanan, S. Jayanti, L. Maier, S. Tischer, O. Deutschmann, *Chem. Eng. Sci.* **2011**, *66* (21), 5184–5191. DOI: <https://doi.org/10.1016/j.ces.2011.07.007>
- [49] P. K. Chaudhary, G. Deo, *Colloids Surf., A* **2022**, *646*, 128973. DOI: <https://doi.org/10.1016/j.colsurfa.2022.128973>
- [50] Z. Zhang, Y. Tian, L. Zhang, S. Hu, J. Xiang, Y. Wang, L. Xu, Q. Liu, S. Zhang, X. Hu, *Int. J. Hydrogen Energy* **2019**, *44* (18), 9291–9306. DOI: <https://doi.org/10.1016/j.ijhydene.2019.02.129>
- [51] H. Zhu, C. Karakaya, R. J. Kee, *Int. J. Green Energy* **2022**, *19* (14), 1568–1582. DOI: <https://doi.org/10.1080/15435075.2021.2018321>
- [52] H. Gossler, L. Maier, S. Angeli, S. Tischer, O. Deutschmann, *Catalysts* **2019**, *9* (3), 227. DOI: <https://doi.org/10.3390/catal9030227>
- [53] H. Gossler, L. Maier, S. Angeli, S. Tischer, O. Deutschmann, *Phys. Chem. Chem. Phys.* **2018**, *20* (16), 10857–10876. DOI: <https://doi.org/10.1039/C7CP07777G>
- [54] J. H. Cho, S. H. An, T.-S. Chang, C.-H. Shin, *Catal Lett.* **2016**, *146* (4), 811–819. DOI: <https://doi.org/10.1007/s10562-016-1695-8>
- [55] K. Okura, T. Okanishi, H. Muroyama, T. Matsui, K. Eguchi, *ChemCatChem* **2016**, *8* (18), 2988–2995. DOI: <https://doi.org/10.1002/cctc.201600610>
- [56] P. Kim, J. B. Joo, H. Kim, W. Kim, Y. Kim, I. K. Song, J. Yi, *Catal Lett.* **2005**, *104* (3–4), 181–189. DOI: <https://doi.org/10.1007/s10562-005-7949-5>
- [57] P. Vacharapong, S. Arayawate, S. Henpraserttae, S. Katanyutanon, S. Charojrochkul, L. Lawtrakul, P. Toochinda, *ChemistrySelect* **2019**, *4* (40), 11913–11919. DOI: <https://doi.org/10.1002/slct.201902663>
- [58] K. Okura, K. Miyazaki, H. Muroyama, T. Matsui, K. Eguchi, *RSC Adv.* **2018**, *8* (56), 32102–32110. DOI: <https://doi.org/10.1039/C8RA06100A>
- [59] S. Henpraserttae, S. Charojrochkul, W. Klysubun, L. Lawtrakul, P. Toochinda, *Catal. Lett.* **2018**, *148* (6), 1775–1783. DOI: <https://doi.org/10.1007/s10562-018-2381-9>
- [60] J. C. Ganley, F. S. Thomas, E. G. Seebauer, R. I. Masel, *Catal. Lett.* **2004**, *96* (3/4), 117–122. DOI: <https://doi.org/10.1023/B:CATL.0000030108.50691.d4>